Contents lists available at ScienceDirect

International Journal of Rock Mechanics and Mining Sciences

journal homepage: www.elsevier.com/locate/ijrmms

# Combined acoustical-electrical modeling for tight sandstones verified by laboratory measurements

Mengqiang Pang [a,b], Jing Ba [a,*], José M. Carcione [a,c], Erik H. Saenger [b,d,e]

[a] School of Earth Sciences and Engineering, Hohai University, Nanjing, 211100, China
[b] Hochschule Bochum, Am Hochschulcampus 1, D-44801, Bochum, Germany
[c] National Institute of Oceanography and Applied Geophysics – OGS, Trieste, 34010, Italy
[d] Fraunhofer IEG - Institution for Energy Infrastructures and Geothermal Energy, Am Hochschulcampus 1, 44801, Bochum, Germany
[e] Institute of Geology, Mineralogy, and Geophysics, Ruhr-University Bochum, Universitätsstrasse 150, 44801, Bochum, Germany

ARTICLE INFO

*Keywords:*
Tight sandstones
Saturation
Pore structure
Wave anelasticity
Electrical conductivity

ABSTRACT

Tight sandstone reservoirs basically have low porosity and permeability, a complex pore structure and a heterogeneous distribution of immiscible fluids. With the development of theoretical models, it is common to characterize rock properties, i.e., pore structure, microfractures, fluid type and saturation, etc., based on acoustic and electrical properties. We have taken four tight sandstone samples and performed X-ray diffraction and cast thin section analyses. We measure porosity and permeability as well as ultrasonic properties and electrical conductivity at different confining pressures and fluid saturations. These measurements show that the P-wave velocity, P-wave attenuation and conductivity strongly depend on the type and saturation of the fluid and the microstructure of the rock. We propose a combined acoustic-electrical model based on the concept of equivalent medium and on the double porosity, patchy saturation and squirt flow models. We then create rock physics templates calibrated with wellbore log data to estimate fluid saturation and equant and soft porosities, which are well corroborated by gas production reports. This work demonstrates the link between combined acoustic-electrical responses and rock properties and provides an effective approach for applications in reservoirs.

## 1. Introduction

Tight-sandstone reservoirs have gradually become the most promising natural gas resources, accounting for 39% of the total reserves and 25% of the total production,[1,2] and their analysis is essential for an effective geological and geophysical characterization.[3–7] These rocks exhibit fabric and fluid distribution heterogeneities, complex pore structures, microfractures and a heterogeneous distribution of immiscible fluids.[8–10]

Experimental and theoretical studies showed that the pore structure, fluid type and saturation affect the wave velocity dispersion and attenuation.[11–18] Recently, the effects of immiscible fluids and pore structure on wave anelasticity were analyzed.[8,9,19–21]

With the development of theoretical models, the effects of pores, microfractures and fluid on rock electrical properties can be investigated.[22–26] Khairy and Harith[27] studied the effects of pore structure, pressure and fluid saturation on the resistivity of sandstones and carbonates based on X-ray diffraction (XRD) and electrical experiments. Yan et al.[28] adopted a digital rock technique and pore morphology to determine the fluid distribution relying on the XRD and CT images, and carried out a sensitivity analysis to obtain the effects of porosity, clay content, temperature, water salinity, heavy minerals, clay type and wettability in low-resistivity oil layers. Li et al.[29] performed high-resolution CT scan, micro scanning images stitching and scanning electron microscopy tests to setup 3D digital cores with multi-mineral components. Then, the electrical responses of tight sandstones, with

* Corresponding author.
*E-mail address:* jba@hhu.edu.cn (J. Ba).

https://doi.org/10.1016/j.ijrmms.2024.105682
Received 9 June 2022; Received in revised form 27 January 2024; Accepted 24 February 2024

**Table 1**
Physical properties of samples.

| Samples | Porosity (%) | Permeability (mD) | Dry-rock density (g/cm$^3$) |
|---|---|---|---|
| A | 7.220 | 0.020 | 2.49 |
| B | 8.998 | 0.078 | 2.41 |
| C | 9.000 | 0.036 | 2.42 |
| D | 10.165 | 0.096 | 2.37 |

**Table 2**
Mineral compositions of the samples.

| Samples | Quartz (%) | Feldspar (%) | Carbonate (%) | Clay (%) | Siderite (%) |
|---|---|---|---|---|---|
| A | 49 | 27 | 18 | 6 | 1 |
| B | 57 | 30 | 8 | 5 | 1 |
| C | 50 | 35 | 7 | 6 | 2 |
| D | 55 | 32 | 7 | 5 | 1 |

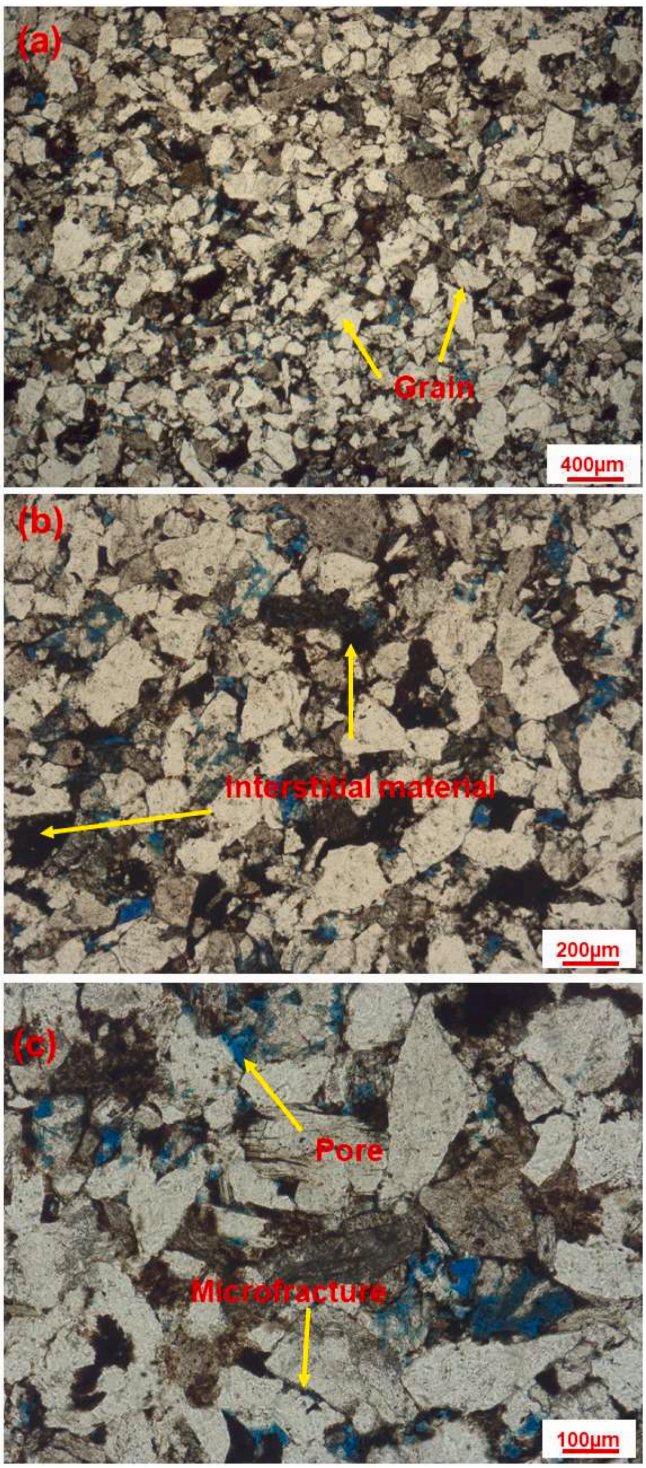


**Fig. 1.** CTSs of sample B at different magnifications.

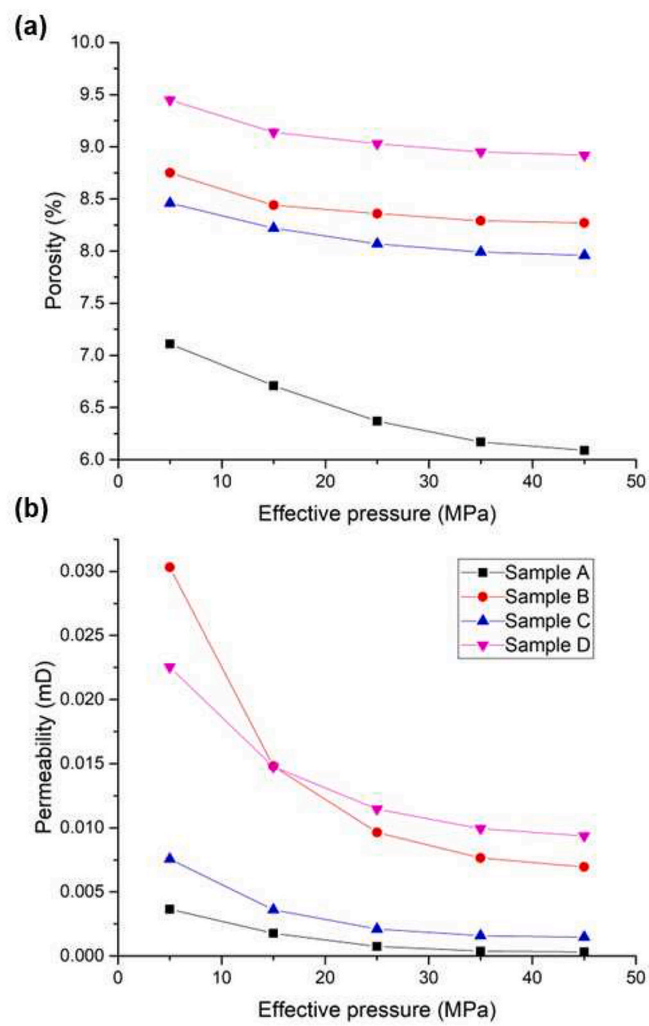


**Fig. 2.** Porosity (a) and permeability (b) of the samples as a function of effective pressure.

low water saturation and complex pore structures, were illustrated by using the finite element method.

Rock-physics modeling based on joint acoustical-electrical properties can reduce the uncertainty of rock characterization/interpretation.[7,30–32] Moreover, researchers have used cross-property relations to characterize rocks.[34–41] Han[42] combined laboratory experiments and models, showing how the wave velocity is related to the electrical conductivity. Cilli and Chapman[33] developed an electrical differential equivalent-medium (DEM) theory and combined it with the elastic version to simulate the properties of sandstones.

There are relatively few studies regarding the acoustical and electrical joint properties of partially-saturated tight rocks, in particular considering attenuation. We have performed XRD experiments, casting of thin sections (CTSs), and porosity and permeability pressure-dependent (PPPD) measurements, and ultrasonic and conductivity

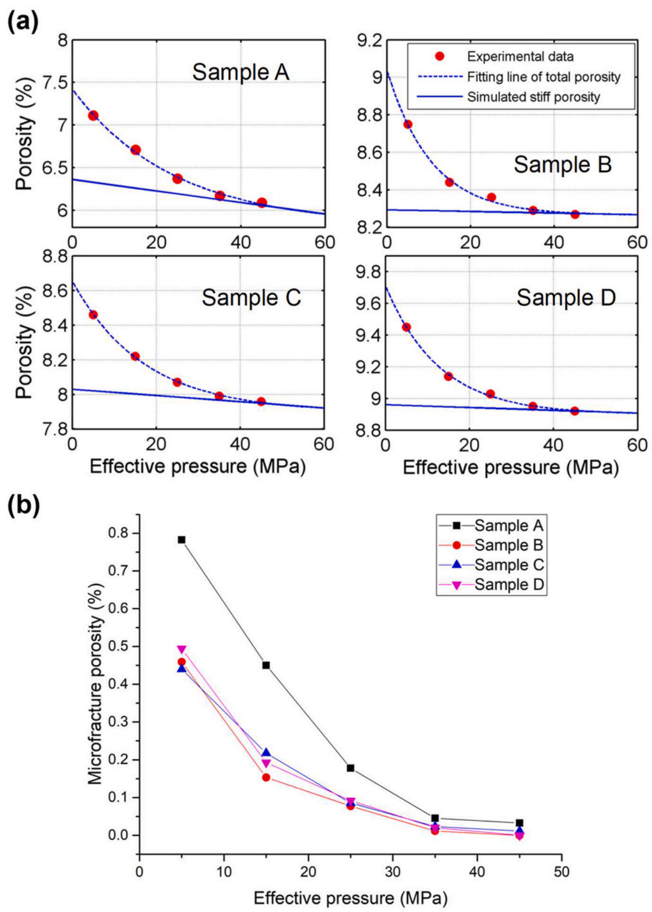


**Fig. 3.** Total and stiff porosities (a) and microfracture porosity (b) as a function of the effective pressure.

experiments at different pressures and saturations. The pore structure, mineral composition, microfracture porosity, wave velocity, attenuation and conductivity of the samples are analyzed, and their relations are discussed.

Three theoretical models are combined, namely, the double-porosity,[43–46] the patchy saturation[47–52] and the squirt flow.[53–57] Then, a joint acoustical-electrical model for tight sandstone is developed by combining several sorts of petrophysical experiments to analyze the effects of pore structure, and fluid type and saturation on the wave velocity, attenuation and conductivity. Finally, we are building an acoustic-electrical rock physics template that will be calibrated against borehole data for use in the characterization of tight sandstone reservoirs.

## 2. Laboratory experiments

In order to analyze the acoustic and electrical properties of partially saturated (gas-water) rocks with complex pore structures, four low clay-content tight-sandstone samples (A-D) are collected. The samples are processed as cylinders with diameters and lengths in the ranges 25.08–25.13 mm and 49.09–49.77 mm, respectively. Their properties are shown in Table 1. CTS, XRD and PPPD measurements are performed, and by applying different confining pressures and fluid saturations, we obtain the ultrasonic P-wave (0.55 MHz) and conductivity (120 Hz) to analyze the effects of microfractures and fluids on the acoustical and electrical properties.

### 2.1. CTS, XRD and PPPD tests

Fig. 1 shows the CTSs of sample B at different magnifications. The rock space mainly includes intergranular pores, dissolved pores and microfractures. Table 2 gives the mineral compositions, which are dominated by quartz, feldspar and carbonates, with a small amount of clay and siderite. The quartz content is high, the feldspar is plagioclase and K-feldspar, and the clays are mainly laumonite and chlorite. We measure the porosity and permeability at confining pressures of 20, 30, 40, 50 and 60 MPa and a pore pressure of 15 MPa. Fig. 2 shows the porosity and permeability measurements, indicating a decrease with effective pressure (confining minus pore), particularly the permeability. The behavior is exponential and then linear with pressure, as described by Shapiro,[58] who expresses the total porosity as

$$\varphi = \varphi_S + \varphi_C, \tag{1}$$

where the stiff porosity ($\varphi_S$) decreases linearly with pressure, while the microfracture porosity ($\varphi_C$) decreases exponentially.

As the effective pressure increases, microfractures close until only the stiff pores remain.[58] Fig. 3a shows the total porosity as a function of the effective pressure, with an exponential fit and a linear fit at high pressures to establish a linear extrapolation and obtain the stiff porosity at different pressures. Then, the microfracture porosity can be obtained (see Fig. 3b), which decreases exponentially with pressure. Sample A with the lowest porosity has the highest microfracture porosity, while the other samples have a similar microfracture porosity, with a trend that deviates from the overall porosity. From this it can be concluded that there is no correlation between the two porosities.

### 2.2. Ultrasonic wave experiments

The wave velocity in the samples is measured by using the ultrasonic pulse method, with a frequency of 0.55 MHz. The experiment is performed at a temperature of 25 °C and pore pressure of 15 MPa. The specimens are placed in an oven for drying and saturated with water in a pressurized device. Water is gradually injected into the sample under pressure, and saturation is determined based on the injection volume. Approximately 20%, 40%, 60%, 80% and 100% water are injected and the samples are sealed with rubber jackets. The samples at each saturation are subjected to confining pressures as indicated above and ultrasonic P wave experiments are performed, to record the waveforms.

The onset of the waveforms is used to calculate the P-wave velocity and the spectral ratio method to estimate the wave attenuation by using aluminium blocks with high quality factors ($Q$) as reference materials,[16,59] as follows,

$$\ln\left[\frac{A_1(f)}{A_2(f)}\right] = -\frac{\pi x}{QV}f + \ln\left[\frac{G_1(f)}{G_2(f)}\right], \tag{2}$$

where $f$ is the frequency, $G_1(f)/G_2(f)$ and $A_1(f)/A_2(f)$ are geometric factors and amplitude spectra of the sample and reference medium, respectively, $x$ is the distance of propagation and $V$ is the wave velocity.

### 2.3. Electrical conductivity experiments

The electrical tests are performed by using the experimental device.[60] The conductivity is measured with alternating currents at a frequency of 120 Hz and a voltage of 1 V. The temperature is 25 °C and the

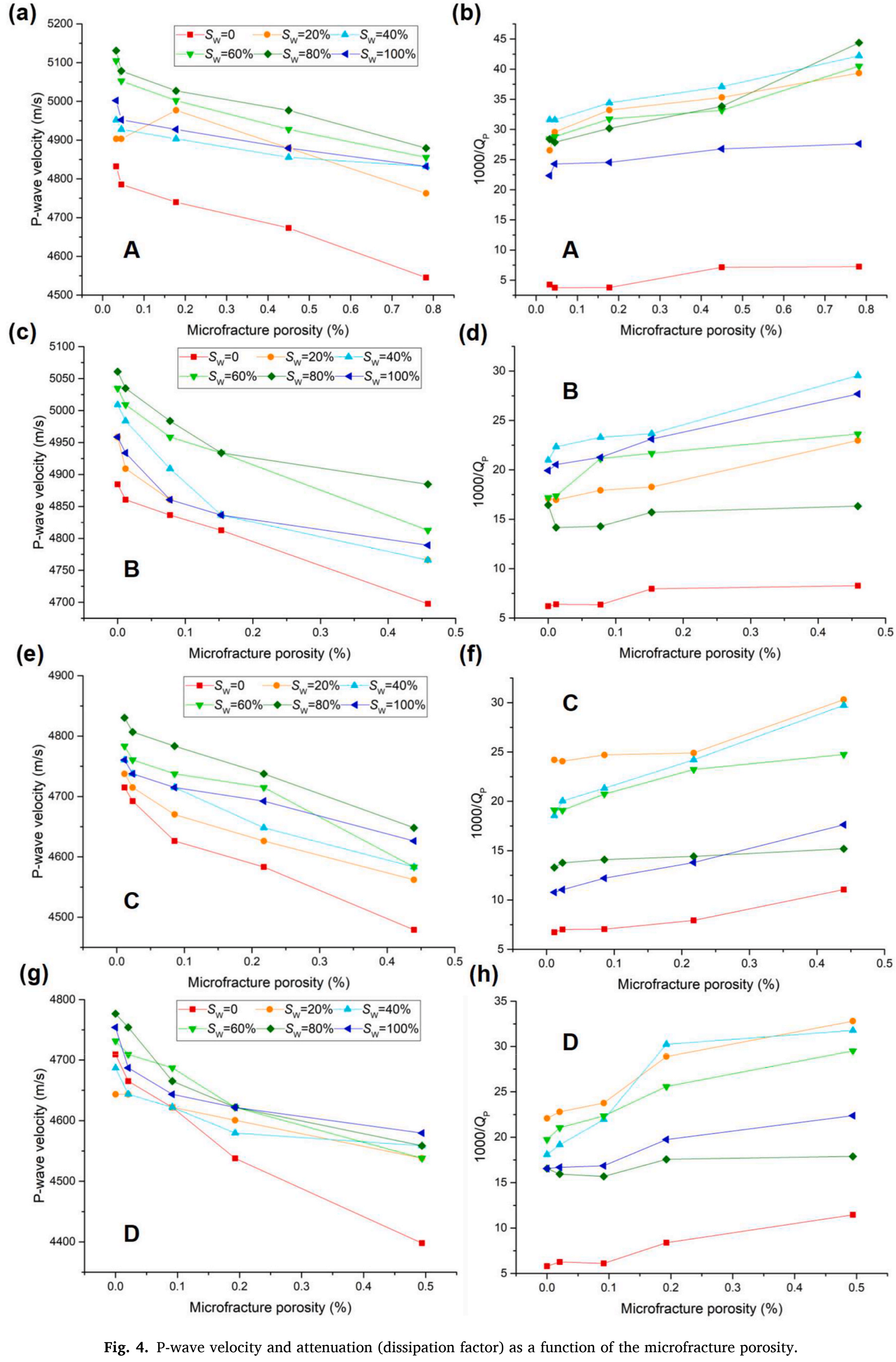


**Fig. 4.** P-wave velocity and attenuation (dissipation factor) as a function of the microfracture porosity.

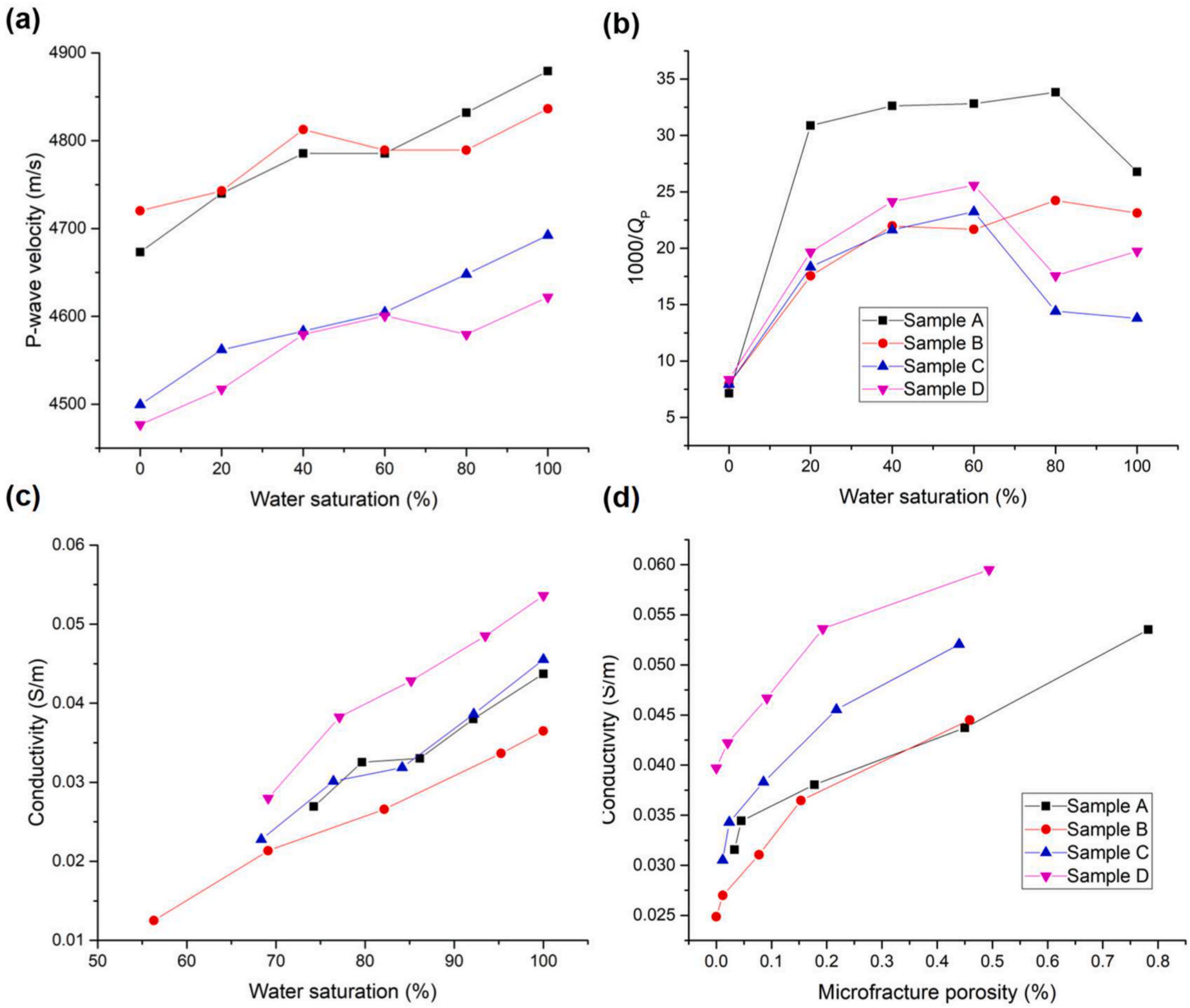


**Fig. 5.** P-wave velocity (a), attenuation (b) and conductivity (c) (with an effective pressure of 15 MPa) as a function of water saturation. (d) Conductivity (full water saturation) as a function of microfracture (soft) porosity.

pore pressure is 15 MPa. First, the samples are fully saturated with brine (salinity 56.5 g/L), placed into the device. and the above confining pressures are applied to measure the resistance. Then, the confining and pore pressures are set at 30 MPa and 15 MPa respectively, and the conductivity is measured at different water saturations. The conductivity $\sigma$ (reciprocal of resistivity $Rt$) can be estimated as

$$Rt = \frac{RS}{L}, \sigma = \frac{1}{Rt}, \tag{3}$$

where $R$ is the resistance of the sample, $L$ is its length and $S$ is the cross-sectional area.

### 2.4. Acoustic and electrical properties

Fig. 4 shows the P-wave velocity and attenuation at different water saturations as a function of the microfracture porosity. The velocity decreases with increasing porosity and attenuation increases. With the increase of water saturation, velocity increases, and the velocity difference between the gas- and water-saturated samples becomes larger with the increase of porosity. The attenuation initially increases and then decreases with water saturation. This phenomenon is attributed to the wave-induced local fluid flow (WILFF), which causes the velocity dispersion and energy attenuation at partial saturation states. When the water saturation approaches 1, the WILFF becomes weaker, which leads to a decrease in attenuation.

Next, we consider an effective pressure of 15 MPa (in situ condition). Fig. 5a and b shows the acoustic properties as a function of water saturation, and Fig. 5c and d the electrical properties as a function of saturation and soft porosity, respectively. Velocity increases with saturation, as expected, and attenuation first increases and then decreases, reaching a maximum value at high saturation. Sample A has the lowest porosity but the highest attenuation, which can be explained by its high microfracture porosity (Fig. 3). Conductivity increases monotonously with saturation and porosity, showing exponential and linear trends. The results show that the acoustical and electrical properties are highly dependent on soft porosity and saturation.

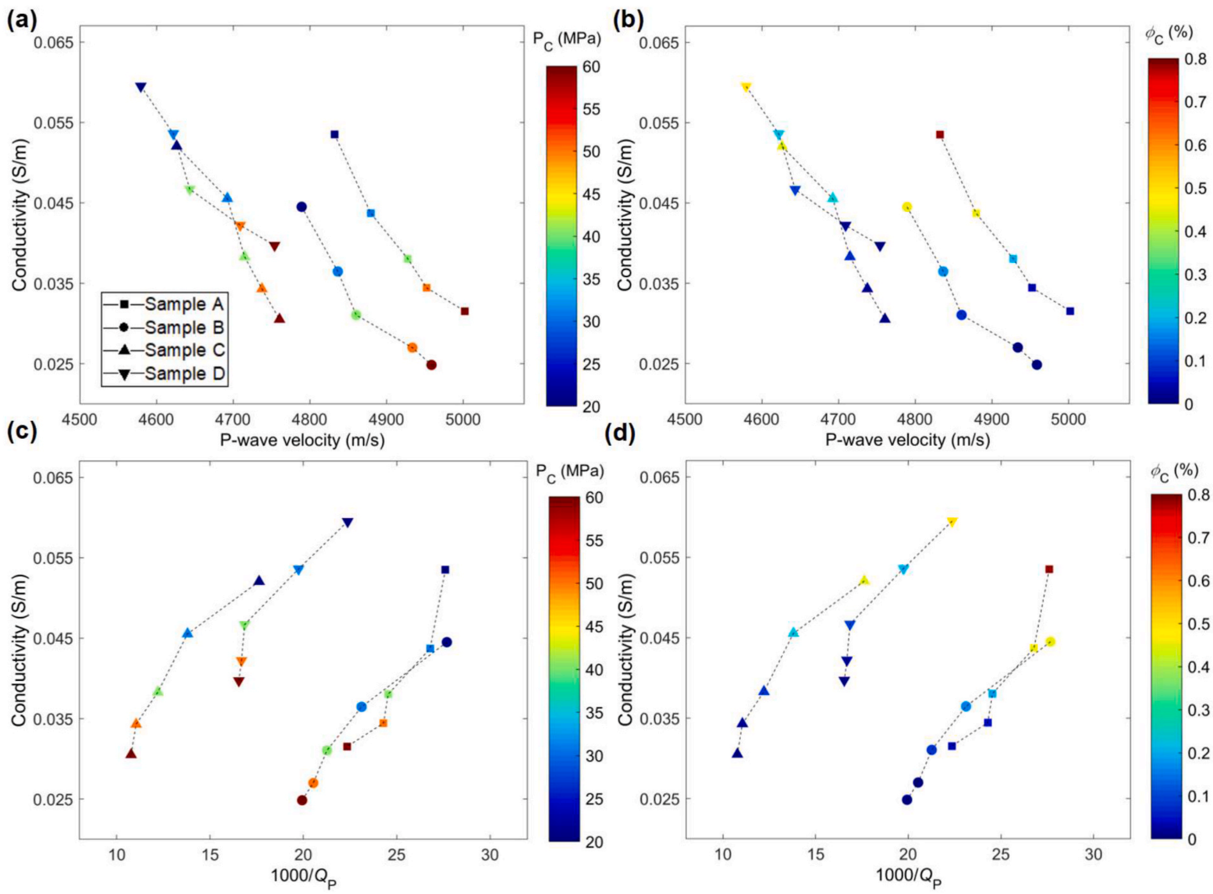


**Fig. 6.** Cross-property relations between conductivity and velocity (a and b), and conductivity and attenuation (c and d) dependent on confining pressure and microfracture porosity.

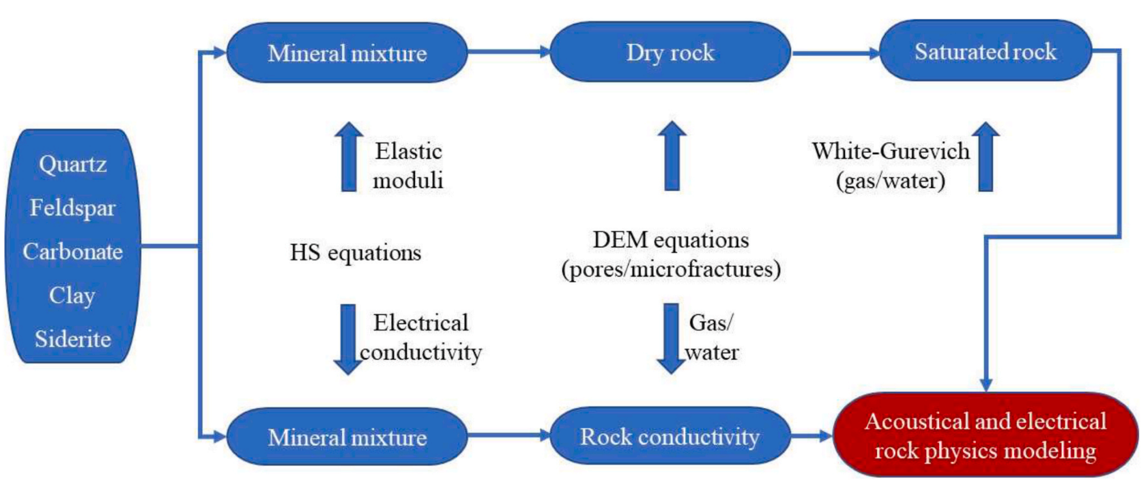


**Fig. 7.** Flow chart of a tight-sandstone acoustical and electrical rock physics modeling.

Fig. 6 shows the cross-property relations. High conductivity is associated with low velocity and high attenuation, and the velocity is higher for higher pressure and lower microfracture porosity, while the attenuation and conductivity are lower.

## 3. Theories and methods

Fig. 7 shows the theoretical scheme to build the joint rock-physics model (RPM), which combines the elastic and electrical equations of Hashin-Shtrikman (HS), DEM and wave propagation. P-wave velocity, attenuation and conductivity, which are affected by the pore structure and saturation, are calculated.

### 3.1. Acoustic RPM

The grain properties are those of a mixture of quartz, feldspar, car-

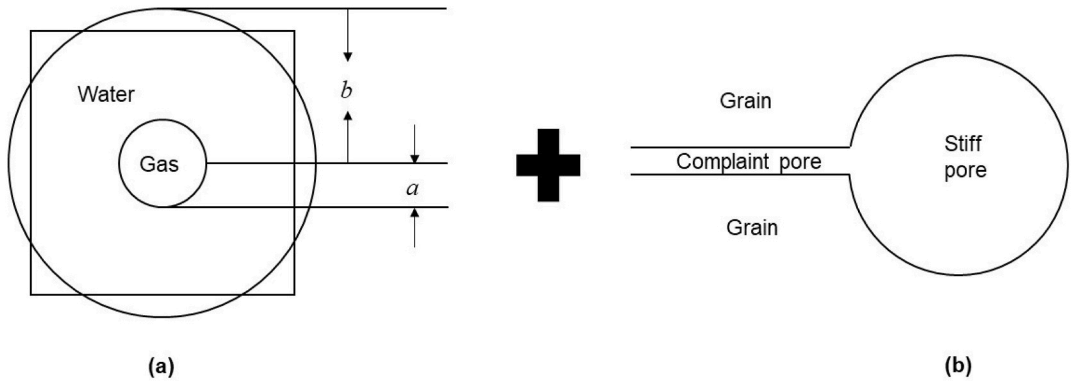


**Fig. 8.** Diagrams showing the White patchy saturation model (a)[48] and squirt-flow model (b).[56]

bonate, clay and siderite based on XRD experiments. The composite bulk modulus is given by the Hashin-Shtrikman (HS,[61]) equations. The complex pore structure of rock samples is analyzed by casting thin sections. The elastic DEM[62] is used to add the pores and microfractures into the mineral mixture to obtain the dry-rock moduli ($K_{dry}$, $\mu_{dry}$),

$$\left(K_2 - K^*_{dry}\right)P^{(*2)}(y) = (1-y)\frac{\mathrm{d}}{\mathrm{dy}}\left[K^*_{dry}(y)\right], \tag{4}$$

$$\left(\mu_2 - \mu^*_{dry}\right)Q^{(*2)}(y) = (1-y)\frac{\mathrm{d}}{\mathrm{dy}}\left[\mu^*_{dry}(y)\right], \tag{5}$$

with initial conditions $K^*_{dry}(0) = K_1$, $\mu^*_{dry}(0) = \mu_1$, where $K_1$ and $\mu_1$ are the bulk and shear moduli of the host material, $y$ is the content of phase 2, and $K_2$ and $\mu_2$ are the corresponding moduli. $P^{*2}$ and $Q^{*2}$ are geometrical factors (Appendix A).

Then, the White and Gurevich models are used to obtain the acous-

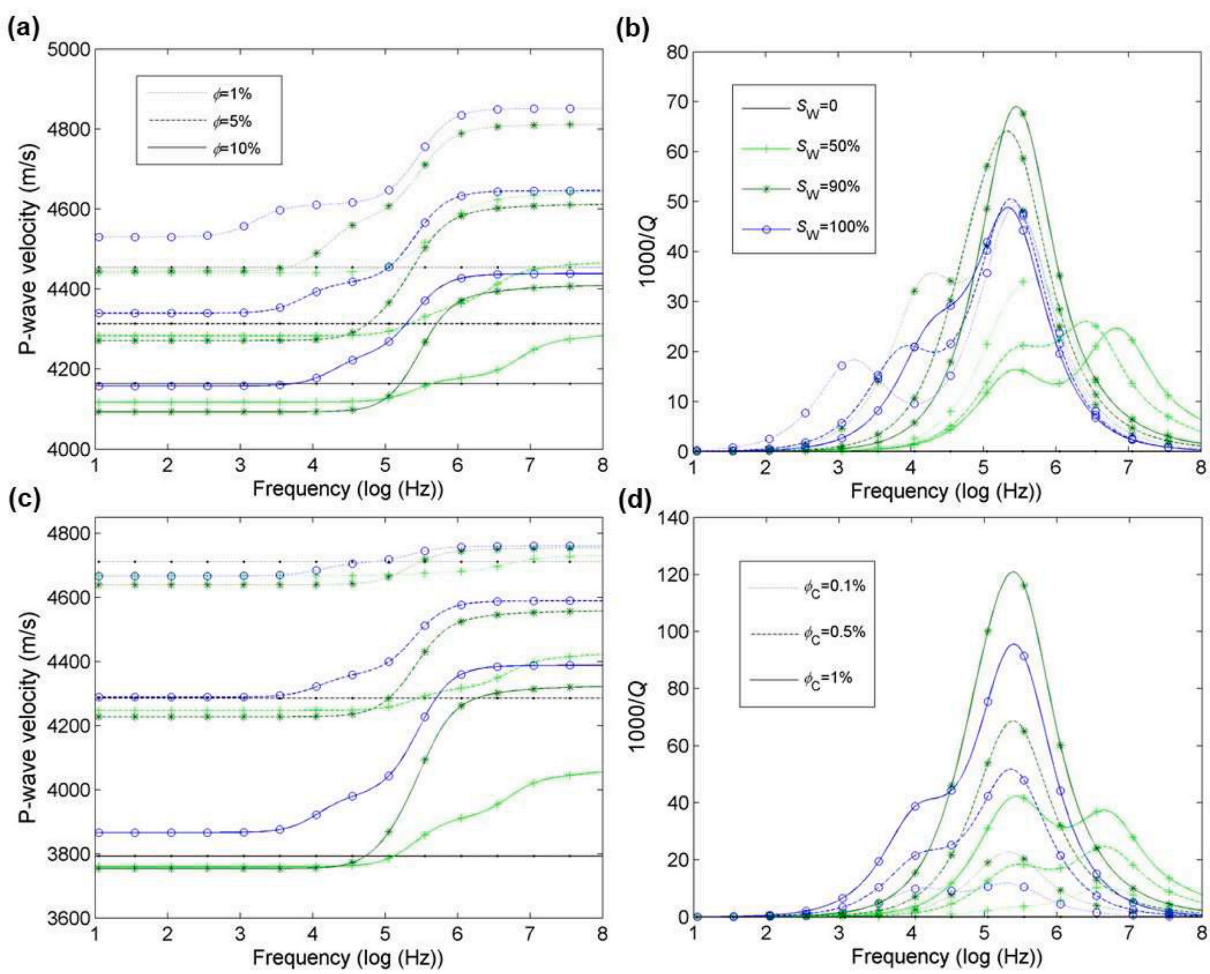


**Fig. 9.** P-wave velocity dispersion and attenuation as a function of frequency at different porosities and saturations (a and b, $\varphi_C = 0.5\%$), and different microfracture porosities and saturations (c and d, $\varphi = 10\%$).

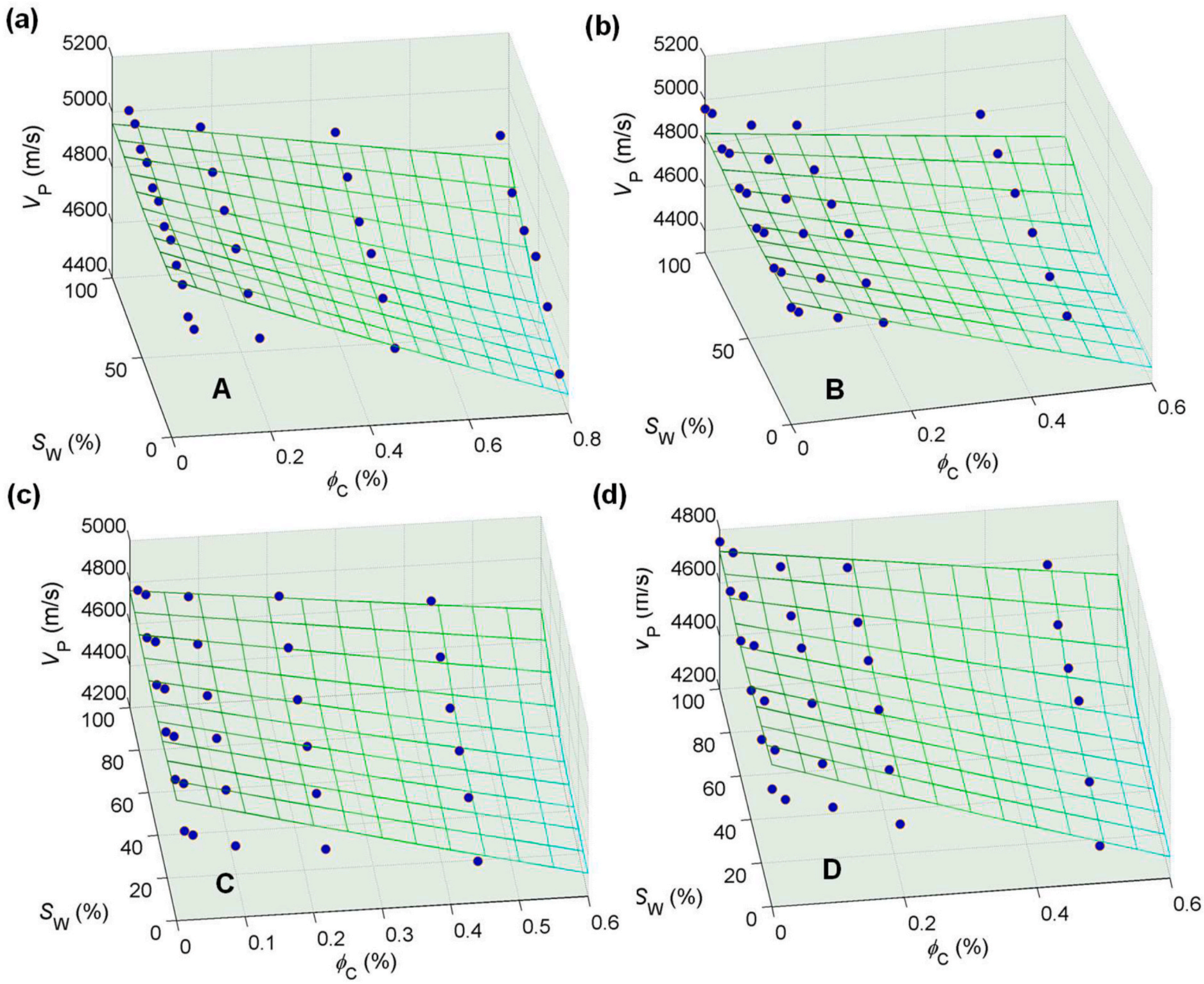


**Fig. 10.** Theoretical P-wave velocity compared with the experimental data. The capital letters indicate the sample.

tical properties of the rock with partial saturation and complex pore structures. Gurevich et al.[56] proposed a squirt-flow model (Fig. 8b), where complaint (soft) pores act as fluid channels to connect stiff pores (see[63]; Section 7.12). The bulk and shear dry-rock moduli, including squirt flow effects, are obtained from

$$\frac{1}{K_{bf}}=\frac{1}{K_h}+\left(\frac{1}{\frac{1}{K_{dry}}-\frac{1}{K_h}}+\frac{3\omega i\eta}{8\varphi_C\alpha_C}\right)^{-1}, \tag{6}$$

$$\frac{1}{\mu_{bf}}=\frac{1}{\mu_{dry}}-\frac{4}{15}\left(\frac{1}{K_{dry}}-\frac{1}{K_{bf}}\right), \tag{7}$$

where $\omega$ is the angular frequency, $\eta$ is fluid viscosity; $\alpha_c$ is the aspect ratio of the microfractures, $K_h$ is the bulk modulus of the skeleton containing only stiff pores, and $K_{dry}$ and $\mu_{dry}$ are the moduli obtained from the DEM equations above.

Finally, the White model is used to estimate the wave response of the saturated rock ([63], Section 7.13). White[47] calculated the dispersion and attenuation caused by a heterogeneous distribution of pore fluid at the mesoscale, based on a spherical fluid distribution of two fluids (gas--water). The model assumes a regular arrangement of cubic elements (radius $b$). The center of each cube unit is a gas-filling sphere with radius $a$, and the outside is a water sphere with radius $b$, as shown in Fig. 8a. Dutta and Odé[48] improved the model and gave a more rigorous equation, which is used in this study. We replace the dry-rock moduli ($K_{dry}$ and $\mu_{dry}$) in the water-saturated area with the moduli ($K_{bf}$, $\mu_{bf}$) containing squirt-flow effects. The equivalent elastic moduli ($K^*$, $\mu^*$) of the partially saturated rock are

$$K^*=\frac{K_\infty}{1-K_\infty W}, \tag{8}$$

$$\mu^*=\frac{1}{2}\left[\left(S_g\mu_{dry}+S_W\mu_{bf}\right)+\left(\frac{1}{S_g/\mu_{dry}+S_W/\mu_{bf}}\right)\right], \tag{9}$$

where

$$K_\infty=\frac{K_2\left(3K_1+4\mu_{bf}\right)+4\mu_{bf}(K_1-K_2)S_g}{\left(3K_1+4\mu_{bf}\right)-3(K_1-K_2)S_g}, \tag{10}$$

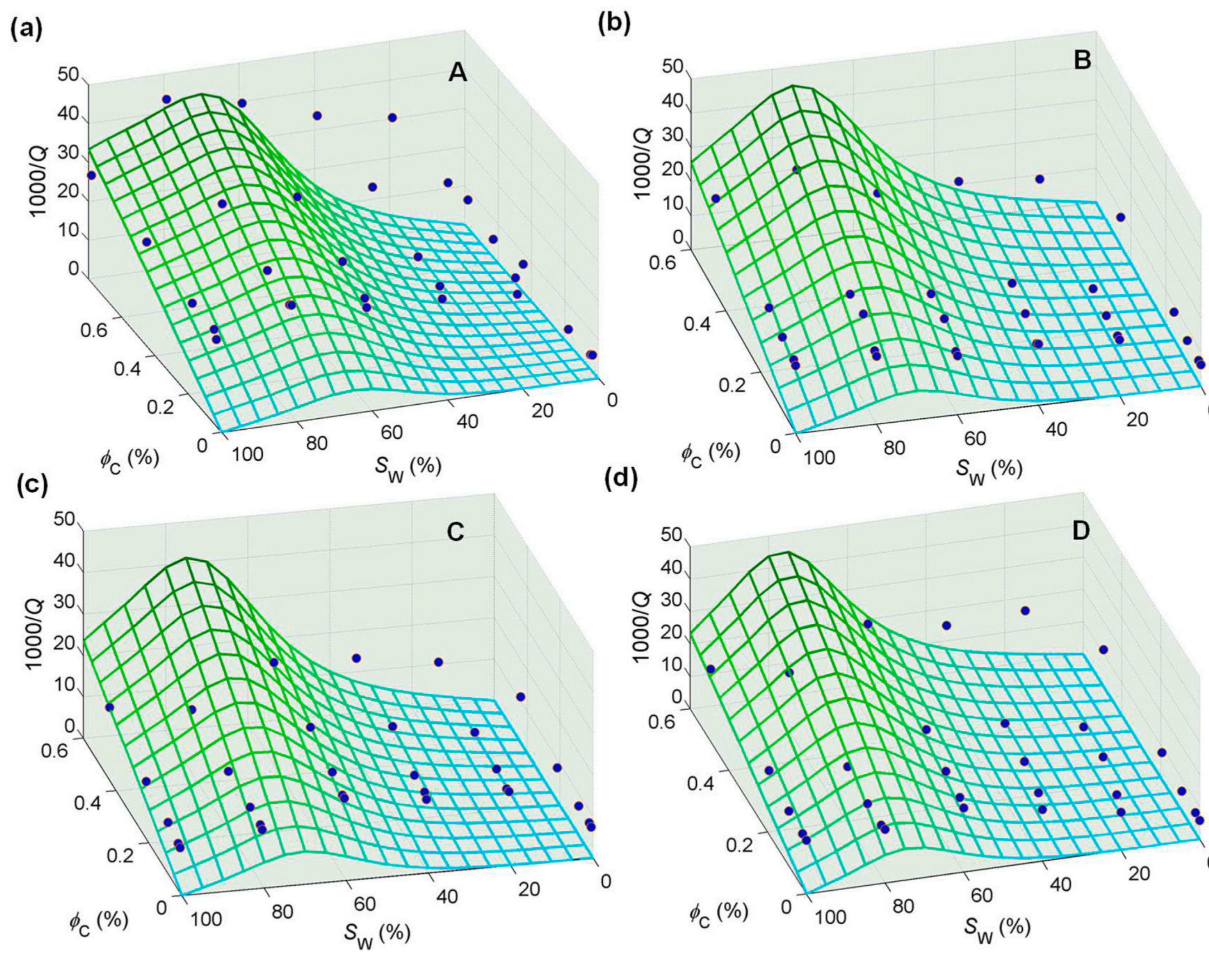


**Fig. 11.** Theoretical attenuation compared with the experimental data. The capital letters indicate the sample.

$$W = \frac{3a^2(R_1 - R_2)(-Q_1 + Q_2)}{b^3\omega i(Z_1 + Z_2)}, \tag{11}$$

where $K_1$ and $K_2$ are the bulk moduli of the saturated rock in gas and water regions respectively, which can be obtained from Gassmann equation and the coefficients $R_1$, $R_2$, $Q_1$, $Q_2$, $Z_1$, $Z_2$ given in Appendix B.

The P-wave velocity and quality factor are

$$V_P = \left[\mathrm{Re}\left(\frac{1}{v_c}\right)\right]^{-1}, \tag{12}$$

$$Q_P = \frac{\mathrm{Re}(K^* + 4\mu^*/3)}{\mathrm{Im}(K^* + 4\mu^*/3)}, \tag{13}$$

respectively,[63] where the complex velocity is $v_c = \sqrt{(K^* + 4\mu^*/3)/\rho}$, the rock density is $\rho = \rho_s(1-\varphi) + \varphi S_g\rho_g + \varphi S_W\rho_W$, where $\rho_s$, $\rho_g$ and $\rho_W$ are the densities of mineral, gas and wtaer, respectively.

### 3.2. Electrical RPM

The electrical HS equation[64,65] is used to calculate the composite conductivity of the mineral mixture. The conductivity is obtained by adding the two pore types (with fluids) to this mixture by using the electrical DEM,[33]

$$(\sigma_2 - \sigma^*)\lambda = (1-y)\frac{d}{dy}[\sigma^*(y)], \tag{14}$$

with initial conditions $\sigma^*(0) = \sigma_1$, where $\sigma_1$ is the conductivity of the host phase, and $\sigma_2$ is the conductivity of phase 2. $y$ is the corresponding content, and

$$\lambda = \frac{1}{3}\sum_{p=1}^{3}\left\{\left[1 + \left(\frac{\sigma_2}{\sigma^*} - 1\right)L_P\right]^{-1}\right\}, \tag{15}$$

where $L_P$ (P = 1, 2, 3) is the depolarizing factor of phase 2.[66,67] We consider ellipsoid inclusions of aspect ratio $\alpha < 1$,

$$L_3 = \frac{1}{1-\alpha^2} - \frac{\alpha}{(1-\alpha^2)^{3/2}}\cos^{-1}\alpha, \tag{16}$$

$$L_1 = L_2 = (1 - L_3)/2, \tag{17}$$

According to Archie's equation,[68] the conductivity of pores and microfractures as a function of water saturation is[60,69]

$$\sigma_2 = \beta^{-1}S_W^n\sigma_W. \tag{18}$$

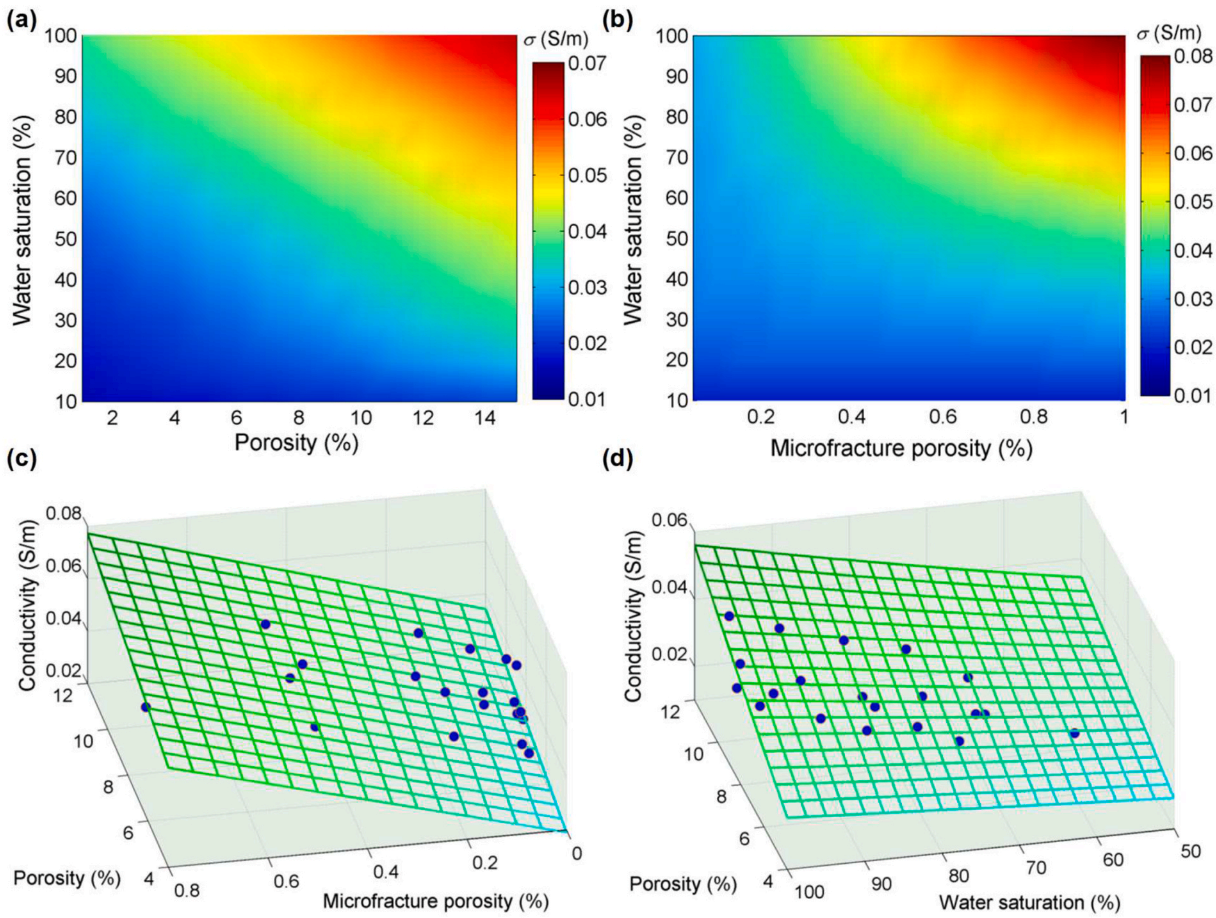


**Fig. 12.** Conductivity as a function of water saturation and porosity (a) ($\varphi_C = 0.5\%$), and microfracture porosity (b) ($\varphi = 10\%$), and theoretical conductivity compared to the experimental data as a function of total and microfracture porosities (c) and water saturation and porosity (d).

where $\sigma_W$ is the brine conductivity, $n$ is a saturation exponent and $\beta$ is a lithology coefficient.

## 4. Model and data

### 4.1. Acoustic response and experimental data

The acoustic RPM yields the P-wave velocity dispersion and attenuation. The bulk and shear moduli and density of the mineral are 35 GPa, 40 GPa and 2.65 g/cm$^3$, respectively, the bulk moduli of gas and water are 0.018 GPa and 2.24 GPa, the densities are 0.09 g/cm$^3$ and 1.002 g/cm$^3$, and the viscosities are 1.6 *10$^{-5}$ Pa s and 9.8 *10$^{-4}$ Pa s, respectively. The aspect ratios of pores and microfractures are 0.2 and 0.001, respectively, and the patch radius $a$ is 0.8 mm.

Fig. 9 shows the velocity and attenuation as a function of frequency, where the typical inflexion points and peaks can be observed. The velocity decreases with porosity and saturation, and attenuation increases with porosity, showing a significant dependence on the soft (microfracture) porosity. Figs. 10 and 11 compare the theoretical and experimental data, showing good agreement, with the exception of sample A with a high microfracture porosity (its attenuation is higher than the model result). The rock structure and fluid distribution become increasingly complicated when the rock has a high microfracture porosity, which is characterized by the multiscale distribution of fluid patches and multiple pore types of the rock structure. The model in this study assumes constant patch size and relatively simplified pore geometries, which could explain the lower attenuation observed in the model compared to sample A.

### 4.2. Electrical response and experimental data

In this case, we assume that the electrical conductivity of brine and mineral are 8.7 S/m and 0.015 S/m, the pore and microfracture aspect ratio are 0.2 and 0.001, and $n$ and $\beta$ are 2 and 1, respectively. Fig. 12a and b shows the rock conductivity, which increases with the soft porosity and saturation. Fig. 12c compares theory and experimental data, where we can see a good agreement. Setting the soft porosity to 5% of the total porosity, we observe the behavior shown in Fig. 12d, where the conductivity increases gradually with porosity and saturation, and model is consistent with the data.

## 5. Example of field data

### 5.1. Geological characteristics and well-log data

The formation is located in the X area of the western depression in

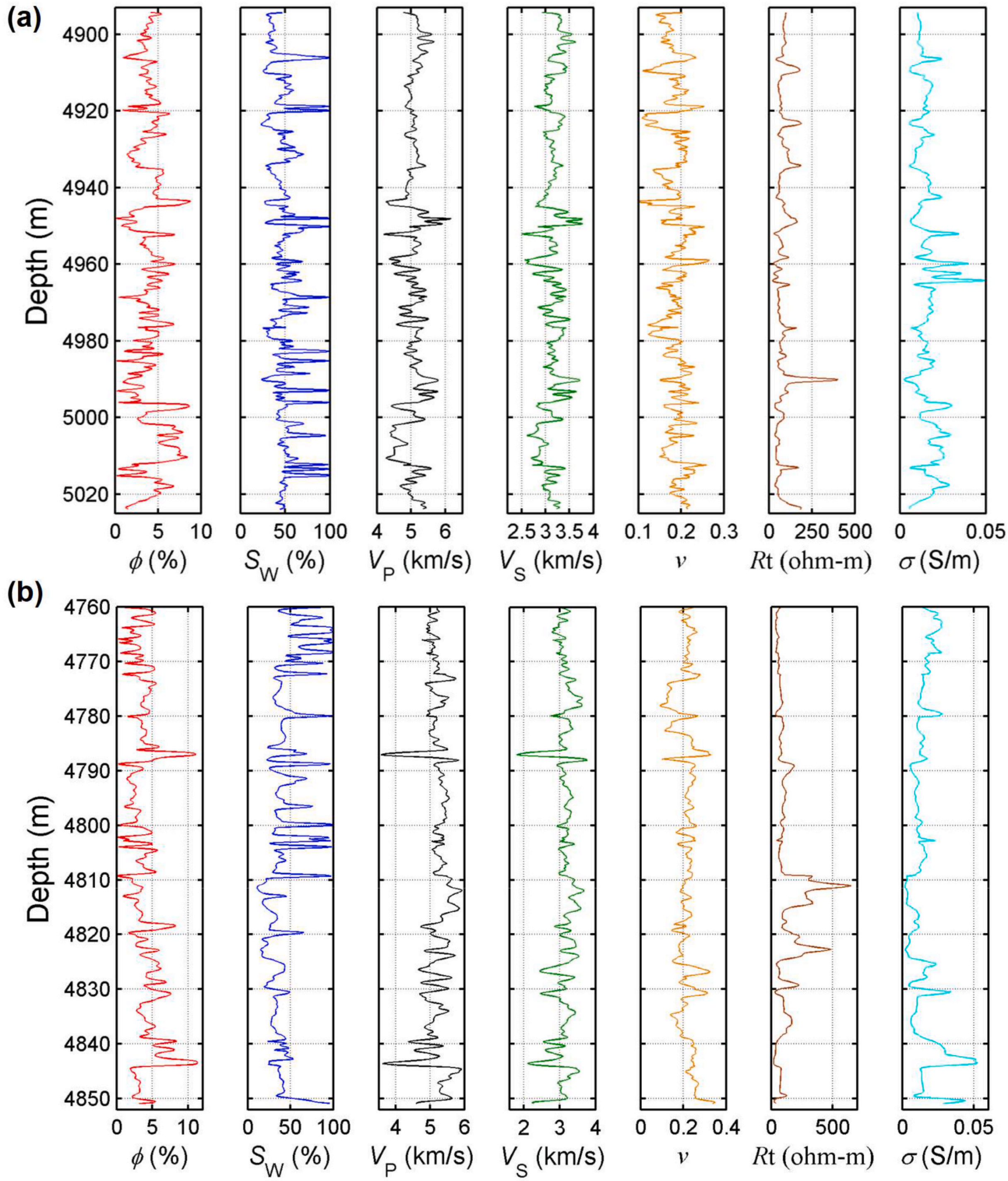


**Fig. 13.** Petrophysical properties of Wells A (a) and B (b).

the Sichuan Basin, China, which is rich in natural gas resources. The tight-sandstone reservoirs mainly produce gas in the Xujiahe Formation of Upper Triassic, with a deep burial. The reservoir is a delta sedimentary system, and the mineral composition is mainly quartz, feldspar, carbonate and clay. The size of the mineral particles is mainly medium to fine, the sorting is good, and the particles are poorly rounded.[3,70] The target reservoir has experienced a strong diagenesis, resulting in low porosity and permeability, diverse pore types and a heterogeneous

**Table 3**
Acoustical and electrical properties.

| | | | |
|---|---|---|---|
| Mineral bulk modulus ($K_S$) | 42 GPa | Mineral conductivity ($\sigma_S$) | 0.005 S/m |
| Shear modulus ($\mu_S$) | 45 GPa | Water conductivity ($\sigma_W$) | 8.7 S/m |
| Density ($\rho_S$) | 2.65 g/cm$^3$ | Lithology coefficient ($\beta$) | 1 |
| Gas bulk modulus ($K_{f1}$) | 1.27 GPa | Saturation exponent ($n$) | 2 |
| Viscosity ($\eta_1$) | 0.000016 Pa s | Pore aspect ratio | 0.1 |
| Density ($\rho_g$) | 0.09 g/cm$^3$ | Microfracture aspect ratio | 0.0002 |
| Water bulk modulus ($K_{f2}$) | 2.24 GPa | Total porosity ($\varphi$) | 2%–10% |
| Viscosity ($\eta_2$) | 0.00098 Pa s | Microfracture porosity ($\varphi_C$) | 0.2%–0.7% |
| Density ($\rho_W$) | 1.002 g/cm$^3$ | Water saturation ($S_W$) | 10%–100% |
| Gas patch radius $a$ | 0.8 mm | | |
| Frequency | 10 kHz | | |

distribution of pore fluids.[10,71]

Well data is used to analyze the petrophysical properties of the reservoirs at the log scale. Fig. 13 shows the porosity, water saturation, P- and S-wave velocities, Poisson's ratio, and electrical properties of two wells. The reservoir porosity is low (less than10%), water saturation is higher than 10%, the elastic velocity is high, and the conductivity and resistivity have wide variations.

### 5.2. Acoustical-electrical rock physics template

We build 3D templates based on conductivity, impedance and Poisson's ratio to estimate the saturation and porosities (total and soft). The model properties are given in Table 3. Fig. 14 shows the template compared with well-log data, where the blue, green and red lines are saturation, total porosity and microfracture porosity isolines, respectively, with the ranges given in Table 3. It can be seen that the agreement between theory and well data is good. The latter can be used for calibration of the models and templates.

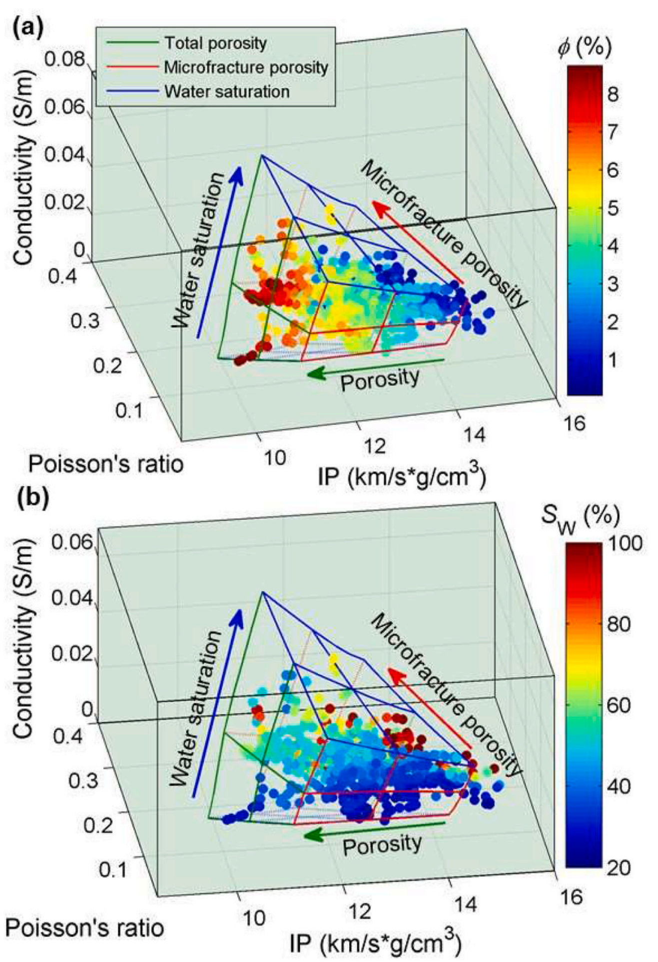


**Fig. 14.** 3D acoustical-electrical template and well-log data. (a) Porosity; (b) Water saturation.

We overlay the acoustical and electrical attributes with the template and use a grid search method to estimate the reservoir properties at wells A and B. These are assigned to the data by minimizing the sum of the squares of the differences between the well-log data and the template results for the three attributes. Fig. 15 compares theoretical and measured log profiles. The results show that water saturation, total and microfracture porosities mainly lie in the ranges 15%–100%, 0–10% and 0–1%, respectively. Well A shows lower porosities and gas saturation than those of Well B. Gas reports indicate that Well A produces 3.6 × 10$^3$ m$^3$ per day of gas and 282 m$^3$ per day of water, and Well B is a high-production gas well, with a value of 1.012 × 10$^6$ m$^3$ per day and a water production of 9.5 m$^3$ per day, which are consistent with the theoretical values.

## 6. Conclusions

Given the complex lithological characteristics of tight sandstones, we develop an acoustical-electrical model and test its performance using the data obtained from four samples at different effective pressures and fluid saturations. The effects of microfracture (soft) porosity and saturation on P-wave velocity, P-wave attenuation and electrical conductivity are determined. The model is based on White's theories of patchy saturation and squirt flow in combination with the elastic and electrical DEM equations describing wave anelasticity (loss and velocity dispersion) at the meso and pore scales, respectively.

The results show that the properties depend significantly on the rock microstructure and saturating fluid. We create 3D rock physics templates based on acoustic and electrical properties and apply them to a tight-sandstone reservoir in the Sichuan Basin. The estimated reservoir properties agree well with the log data and are confirmed by the gas production reports. This study demonstrates the link between acoustical-electrical properties, rock microstructure and fluids and provides an effective approach for reservoir interpretation based on the joint properties.

### CRediT authorship contribution statement

**Mengqiang Pang:** Conceptualization, Methodology, Writing – original draft, Formal analysis, Investigation, Validation. **Jing Ba:** Data curation, Resources, Writing – review & editing, Conceptualization, Formal analysis, Funding acquisition, Investigation, Methodology, Project administration, Supervision, Validation, Writing – original draft. **José M. Carcione:** Writing – review & editing, Formal analysis, Investigation, Supervision. **Erik H. Saenger:** Writing – review & editing,

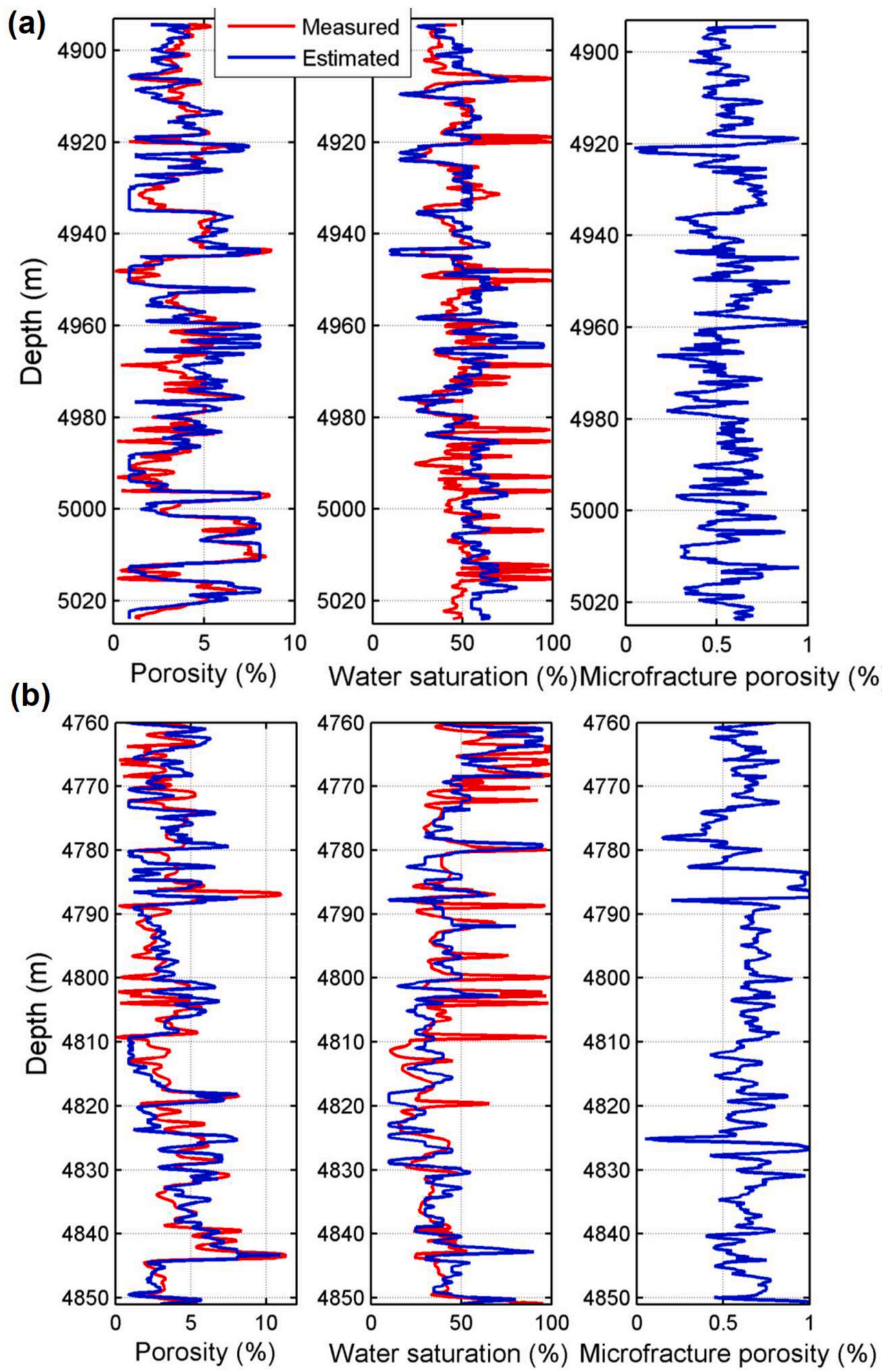


**Fig. 15.** Theoretical and experimental profiles of Wells A (a) and B (b).

Investigation, Resources, Validation.

### Declaration of competing interest

The authors declare that they have no known competing financial interests or personal relationships that could have appeared to influence the work reported in this paper.

### Data availability

Data will be made available on request.

### Acknowledgements

This work is supported by the National Natural Science Foundation of China (grant no. 41974123, 42174161) and the Jiangsu Province Science Fund for Distinguished Young Scholars (grant no. BK20200021). Experimental waveform and electrical data associated with this article can be accessed at https://zenodo.org/record/6612870.

## Appendix A. Geometrical factors *P* and *Q*

The coefficients $P$ and $Q$ for ellipsoidal inclusions are given in Berryman[72] and Mavko et al.,[65]

$$P = \frac{1}{3}T_1, Q = \frac{1}{5}\left(T_2 - \frac{1}{3}T_1\right), \tag{A-1}$$

with

$$T_1 = \frac{3F_1}{F_2}, T_2 - \frac{1}{3}T_1 = \frac{2}{F_3} + \frac{1}{F_4} + \frac{F_4F_5 + F_6F_7 - F_8F_9}{F_2F_4}, \tag{A-2}$$

where

$$F_1 = 1 + G\left[\frac{3}{2}(g+\theta) - J\left(\frac{3}{2}g + \frac{5}{2}\theta - \frac{4}{3}\right)\right], \tag{A-3}$$

$$F_2 = 1 + G\left[1 + \frac{3}{2}(g+\theta) - \frac{J}{2}(3g+5\theta)\right] + H(3-4J) + \frac{G}{2}(G+3H)(3-4J)\left[g+\theta - J\left(g - \theta + 2\theta^2\right)\right], \tag{A-4}$$

$$F_3 = 1 + G\left[1 - \left(g + \frac{3}{2}\theta\right) + J(g+\theta)\right], \tag{A-5}$$

$$F_4 = 1 + \frac{G}{4}[g + 3\theta - J(g-\theta)], \tag{A-6}$$

$$F_5 = G\left[-g + J\left(g + \theta - \frac{4}{3}\right) + H\theta(3-4J)\right], \tag{A-7}$$

$$F_6 = 1 + G[1 + g - J(g+\theta) + H(1-\theta)(3-4J)], \tag{A-8}$$

$$F_7 = 2 + \frac{G}{4}[3g + 9\theta - J(3g+5\theta)] + H\theta(3-4J), \tag{A-9}$$

$$F_8 = G\left[1 - 2J + \frac{g}{2}(J-1) + \frac{\theta}{2}(5J-3)\right] + H(1-\theta)(3-4J), \tag{A-10}$$

$$F_9 = G[(J-1)g - J\theta] + H\theta(3-4J), \tag{A-11}$$

with

$$G = \mu_i/\mu_m - 1, \tag{A-12}$$

$$H = \frac{1}{3}\left(K_i/K_m - \mu_i/\mu_m\right), \tag{A-13}$$

$$J = \left[(1-2v_m)/2(1-v_m)\right], \tag{A-14}$$

where $K_m$, $\mu_m$ and $v_m$ are the bulk and shear moduli and Poisson's ratio of the host phase, respectively, $K_i$, and $\mu_i$ are the bulk and shear moduli of phase $i$, and

$$\theta = \left\{ \begin{array}{l} \dfrac{\alpha}{(\alpha^2-1)^{3/2}}\left[\alpha\left(\alpha^2-1\right)^{1/2} - \cosh^{-1}\alpha\right] \\ \dfrac{\alpha}{(1-\alpha^2)^{3/2}}\left[\cos^{-1}\alpha - \alpha\left(1-\alpha^2\right)^{1/2}\right] \end{array} \right\}, \tag{A-15}$$

for prolate ($\alpha > 1$) and oblate ($\alpha < 1$) spheroids, respectively, with $\alpha$ the aspect ratio, and

$$g = \frac{\alpha^2}{1-\alpha^2}(3\theta - 2)\ , \tag{A-16}$$

## Appendix B. Coefficients of the White and squirt-flow models

According to Dutta and Odé[48] and Ren et al.,[9] we have

$$K_1 = \frac{K_s - K_{dry} + \varphi K_{dry}\left(K_s/K_{f1} - 1\right)}{1 - \varphi - K_{dry}/K_s + \varphi K_s/K_{f1}}, \tag{B-1}$$

$$K_2 = \frac{K_s - K_{bf} + \varphi K_{bf}\left(K_g/K_{f2} - 1\right)}{1 - \varphi - K_{bf}/K_s + \varphi K_s/K_{f2}}, \tag{B-2}$$

$$R_1 = \frac{K_1 - K_{dry}}{1 - K_{dry}/K_s}\frac{3K_2 + 4\mu_{bf}}{K_2\left(3K_1 + 4\mu_{bf}\right) + 4\mu_{bf}(K_1 - K_2)S_g}, \tag{B-3}$$

$$R_2 = \frac{K_2 - K_{bf}}{1 - K_{bf}/K_s}\frac{3K_1 + 4\mu_1}{K_2\left(3K_1 + 4\mu_{bf}\right) + 4\mu_{bf}(K_1 - K_2)S_g}, \tag{B-4}$$

$$Q_1 = \frac{\left(1 - K_{dry}/K_s\right)K_{A1}}{K_1}, \tag{B-5}$$

$$Q_2 = \frac{\left(1 - K_{bf}/K_s\right)K_{A2}}{K_2}, \tag{B-6}$$

$$Z_1 = \frac{\eta_1 a}{\kappa}\frac{1 - \exp(-2\gamma_1 a)}{(\gamma_1 a - 1) + (\gamma_1 a + 1)\exp(-2\gamma_1 a)}, \tag{B-7}$$

$$Z_2 = -\frac{\eta_2 a}{\kappa}\frac{(\gamma_2 b + 1) + (\gamma_2 b - 1)\exp[2\gamma_2(b-a)]}{(\gamma_2 b + 1)(\gamma_2 a - 1) - (\gamma_2 b - 1)(\gamma_2 a + 1)\exp[2\gamma_2(b-a)]}, \tag{B-8}$$

where $\varphi$ is the porosity, $K_S$ is the bulk modulus of the mineral, $K_{f1}$ and $K_{f2}$ are the bulk moduli of gas and water respectively, $\eta_1$ and $\eta_2$ are the viscosities, and $\kappa$ is the permeability,[65] such that

$$\kappa = \frac{\kappa_0 \varphi_2^3}{(1-\varphi_2)^2}\ , \tag{B-9}$$

$$\gamma_1 = \sqrt{\omega i \eta_1/(\kappa K_{E1})}, \tag{B-10}$$

$$\gamma_2 = \sqrt{\omega i \eta_2/(\kappa K_{E2})}, \tag{B-11}$$

where, $\kappa_0 = 25$ D, and,

$$K_{E1} = \left[1 - \frac{K_{f1}(1 - K_1/K_s)\left(1 - K_{dry}/K_s\right)}{\varphi K_1\left(1 - K_{f1}/K_s\right)}\right]K_{A1}, \tag{B-12}$$

$$K_{E2} = \left[1 - \frac{K_{f2}(1 - K_2/K_s)\left(1 - K_{bf}/K_s\right)}{\varphi K_2\left(1 - K_{f2}/K_s\right)}\right]K_{A2}, \tag{B-13}$$

$$K_{A1} = \left[\frac{\varphi}{K_{f1}} + \frac{1-\varphi}{K_s} - \frac{K_{dry}}{K_s^2}\right]^{-1}, \tag{B-14}$$

$$K_{A2} = \left[\frac{\varphi}{K_{f2}} + \frac{1-\varphi}{K_s} - \frac{K_{bf}}{K_s^2}\right]^{-1}. \tag{B-15}$$

## References


1. Khlaifat AL, Qutob H, Barakat N. Tight gas sands development is critical to future world energy resources. In: *SPE Middle East Unconventional Gas Conference and Exhibition*. Society of Petroleum Engineers; 2011.
2. Dai J, Ni Y, Gong D, et al. Geochemical characteristics of gases from the largest tight sand gas field (Sulige) and shale gas field (Fuling) in China. *Mar Petrol Geol*. 2017; 79:426–438. https://doi.org/10.1016/j.marpetgeo.2016.10.021.
3. Zhu R, Zou C, Zhang N, et al. Diagenetic fluids evolution and genetic mechanism of tight sandstone gas reservoirs in Upper Triassic Xujiahe Formation in Sichuan Basin, China. *Sci China Earth Sci*. 2008;51(9):1340–1353. https://doi.org/10.1007/s11430-008-0102-8.
4. Ukar E, Laubach SE, Hooker JN. Outcrops as guides to subsurface natural fractures: Example from the Nikanassin Formation tight-gas sandstone, Grande Cache, Alberta foothills, Canada. *Mar Petrol Geol*. 2019;103:255–275.
5. Kadkhodaie R, Moussavi R, Rezaee R, Nabi M, Kadkhodaie A. Seismic inversion and attributes analysis for porosity evaluation of the tight gas sandstones of the Whicher Range field in the Perth Basin, Western Australia. *J Nat Gas Sci Eng*. 2014;21: 1073–1083.
6. Kadkhodaie R, Kadkhodaie A, Rezaee R, Mehdipour V. Unraveling the reservoir heterogeneity of the tight gas sandstones using the porosity conditioned facies modeling in the Whicher Range field, Perth Basin, Western Australia. *J Petrol Sci Eng*. 2019;176:97–115.
7. Kadkhodaie R, Kadkhodaie A, Rezaee R. Study of pore system properties of tight gas sandstones based on analysis of the seismically derived velocity deviation log: a case study from the Perth Basin of western Australia. *J Petrol Sci Eng*. 2021;196, 108077.
8. Li D, Wei J, Di B, Ding P, Huang S, Shuai D. Experimental study and theoretical interpretation of saturation effect on ultrasonic velocity in tight sandstones under different pressure conditions. *Geophys J Int*. 2018;212(3):2226–2237.
9. Ren S, Han T, Fu L. Theoretical and experimental study of P-wave attenuation in partially saturated sandstones under different pressures. *Chin J Geophys*. 2020;63(7): 2722–2736. https://doi.org/10.6038/cjg2020O0021 (in Chinese).
10. Pang M, Ba J, Carcione JM. Characterization of gas saturation in tight-sandstone reservoirs with rock-physics templates based on seismic Q. *J Energy Eng*. 2021;147 (3), 04021011.
11. Müller TM, Gurevich B, Lebedev M. Seismic wave attenuation and dispersion resulting from wave-induced flow in porous rocks-A review. *Geophysics*. 2010;75: 75A147–75A164. https://doi.org/10.1190/1.3463417.
12. Amalokwu K, Best IA, Sothcott J, Chapman M, Minshull T, Li Y. Water saturation effects on elastic wave attenuation in porous rocks with aligned fractures. *Geophys J Int*. 2014;197:943–947.
13. Chapman S, Tisato N, Quintal B, Holliger K. Seismic attenuation in partially saturated Berea sandstone submitted to a range of confining pressures. *J Geophys Res Solid Earth*. 2016;121(3):1664–1676.
14. Picotti S, Carcione JM, Ba J. Rock-physics templates for seismic Q. *Geophysics*. 2018; 84(1):MR13–MR23.
15. Solazzi SG, Guarracino L, Rubino JG, Holliger K. Saturation Hysteresis effects on the seismic Signatures of partially saturated heterogeneous porous rocks. *J Geophys Res*. 2019;124(11):11316–11335.
16. Pang M, Ba J, Carcione JM, Picotti S, Zhou J, Jiang R. Estimation of porosity and fluid saturation in carbonates from rock-physics templates based on seismic Q. *Geophysics*. 2019;84(6):M25–M36. https://doi.org/10.1190/geo2019-0031.1.
17. Zhang L, Ba J, Carcione JM. Wave propagation in infinituple-porosity media. *J Geophys Res Solid Earth*. 2021;126(4), e2020JB021266.
18. Zhang L, Ba J, Carcione JM, Wu C. Seismic wave propagation in partially saturated rocks with a fractal distribution of fluid-patch size. *J Geophys Res Solid Earth*. 2022; 127(2), e2021JB023809.
19. Ba J, Xu W, Fu L, Carcione J, Zhang L. Rock anelasticity due to patchy-saturation and fabric heterogeneity: a double-double porosity model of wave propagation. *J Geophys Res Solid Earth*. 2017;122(3):1949–1976. https://doi.org/10.1002/2016JB013882.
20. Chen Y, Zong Z, Huang C, Zhang S. Seismic wave attenuation and dispersion induced by fluid flow within various cracks and a small amount of bubbly fluid. *Ann Geophys*. 2020;63(4), SE435-SE435.
21. Ma R, Ba J, Lebedev M, Gurevich B, Sun Y. Effect of pore fluid on ultrasonic S-wave attenuation in partially saturated tight rocks. *Int J Rock Mech Min Sci*. 2021;147, 104910.
22. Carcione JM, Seriani G. An electromagnetic modelling tool for the detection of hydrocarbons in the subsoil. *Geophys Prospect*. 2000;48(2):231–256.
23. Ziarani AS, Aguilera R. Pore-throat radius and tortuosity estimation from formation resistivity data for tight-gas sandstone reservoirs. *J Appl Geophys*. 2012;83:65–73.
24. Li M, Tang Y, Bernabé Y, et al. Pore connectivity, electrical conductivity, and partial water saturation: network simulations. *J Geophys Res Solid Earth*. 2015;120(6): 4055–4068.
25. Soleymanzadeh A, Kord S, Monjezi M. A new technique for determining water saturation based on conventional logs using dynamic electrical rock typing. *J Petrol Sci Eng*. 2021;196, 107803.
26. Wang S, Tan M, Wang X, Zhang L. Microscopic response mechanism of electrical properties and saturation model establishment in fractured carbonate rocks. *J Petrol Sci Eng*. 2022;208, 109429.
27. Khairy H, Harith ZZT. Influence of pore geometry, pressure and partial water saturation to electrical properties of reservoir rock: Measurement and model development. *J Petrol Sci Eng*. 2011;78(3-4):687–704.
28. Yan W, Sun J, Zhang J, et al. Studies of electrical properties of low-resistivity sandstones based on digital rock technology. *J Geophys Eng*. 2018;15(1):153–163.
29. Li X, Li C, Li B, Liu X, Chao Y. Response laws of rock electrical property and saturation evaluation method of tight sandstone. *Petrol Explor Dev*. 2020;47(1): 214–224.
30. Jensen EH, Gelius LJ, Johansen TA, Wang Z. Consistent joint elastic-electrical differential effective-medium modelling of compacting reservoir sandstones. *Geophys Prospect*. 2013;61(4):788–802.
31. Gabàs A, Macau A, Benjumea B, et al. Joint audio-magnetotelluric and passive seismic imaging of the Cerdanya Basin. *Surv Geophys*. 2016;37:897–921. https://doi.org/10.1007/s10712-016-9372-4.
32. Cilli P, Chapman M. Modelling the elastic and electrical proper-ties of rocks with complex pore geometries. *80th Annual International Conference and Exhibition, EAGE, Extended Abstracts*. 2018. https://doi.org/10.3997/2214-4609.201801407.
33. Cilli P, Chapman M. Linking elastic and electrical properties of rocks using cross-property DEM. *Geophys J Int*. 2021;225:1812–1823.
34. Carcione JM, Seriani G, Gei D. Acoustic and electromagnetic properties of soils saturated with salt water and NAPL. *J Appl Geophys*. 2003;52(4):177–191.
35. Carcione JM, Ursin B, Nordskag JI. Cross-property relations between electrical conductivity and the seismic velocity of rocks. *Geophysics*. 2007;72(5):E193–E204.
36. Carcione JM, Gei D, Picotti S, Michelini A. Cross-hole electromagnetic and seismic modeling for CO2 detection and monitoring in a saline aquifer. *Journal of petroleum science and engineering*. 2012;100:162–172.
37. Gomez CT, Dvorkin J, Vanorio T. Laboratory measurements of porosity, permeability, resistivity, and velocity on Fontainebleau sandstones. *Geophysics*. 2010;75(6):E191–E204.
38. Han T, Best A, Sothcott J, MacGregor L. Joint elastic-electrical properties of reservoir sandstones and their relationships with petrophysical parameters. *Geophys Prospect*. 2011;59:518–535.
39. Han T, Wei Z, Li F. How the effective pore and grain shapes are correlated in Berea sandstones: Implications for joint elastic-electrical modeling. *Geophysics*. 2020;85 (3):MR147–MR154.
40. Cilli P, Chapman M. The power-law relation between inclusion aspect ratio and porosity: Implications for electrical and elastic modeling. *J Geophys Res Solid Earth*. 2020;125(5):1–25.
41. Pang M, Ba J, Carcione JM, Saenger EH. Elastic-electrical rock-physics template for the characterization of tight-oil reservoir rocks. *Lithosphere*. 2021, 3341849.
42. Han T. Joint elastic-electrical properties of artificial porous sandstone with aligned fractures. *Geophys Res Lett*. 2018;45(7):3051–3058.
43. Pride SR, Berryman JG. Linear dynamics of double-porosity and dual-permeability materials. Part 1: Governing equations and acoustic attenuation. *Phys Rev E*. 2003; 68, 036603. https://doi.org/10.1103/PhysRevE.68.036603.
44. Pride SR, Berryman JG. Linear dynamics of double-porosity and dual-permeability materials: Part II - fluid transport equations. *Phys Rev E*. 2003;68, 036604. https://doi.org/10.1103/PhysRevE.68.036604.
45. Ba J, Carcione JM, Nie J. Biot-Rayleigh theory of wave propagation in double-porosity media. *J Geophys Res*. 2011;116, B06202. https://doi.org/10.1029/2010JB008185.
46. Tang X. A unified theory for elastic wave propagation through porous media containing cracks - an extension of Biot's poroelastic wave theory. *Sci China Earth Sci*. 2011;54:1441–1452. https://doi.org/10.1007/s11430-011-4245-7.
47. White JE. Computed seismic speeds and attenuation in rocks with partial gas saturation. *Geophysics*. 1975;40:224–232. https://doi.org/10.1190/1.1440520.
48. Dutta NC, Odé H. Attenuation and dispersion of compressional waves in fluid-filled porous rocks with partial gas saturation (White model): Part I - Biot theory. *Geophysics*. 1979;44:1777–1788. https://doi.org/10.1190/1.1440938.
49. Carcione JM, Helle HB, Pham NH. White's model for wave propagation in partially saturated rocks: comparison with poroelastic numerical experi-ments. *Geophysics*. 2003;68:1389–1398.
50. Vogelaar B, Smeulders D. Extension of White's layered model to the full frequency range. *Geophys Prospect*. 2007;55:685–695. https://doi.org/10.1111/j.1365-2478.2007.00648.x.
51. Vogelaar B, Smeulders D, Harris J. Exact expression for the effective acoustics of patchy-saturated rocks. *Geophysics*. 2010;75(4):N87–N96. https://doi.org/10.1190/1.3463430.
52. Kobayashi Y, Mavko G. Variation in P-wave modulus with frequency and water saturation: extension of dynamic-equivalent-medium approach. *Geophysics*. 2016;81 (5):D479–D494.
53. Dvorkin J, Nur A. Dynamic poroelasticity: a unified model with the squirt and the Biot mechanisms. *Geophysics*. 1993;58(4):524–533.
54. Chapman M, Zatsepin SV, Crampin S. Derivation of a microstructural poroelastic model. *Geophys J Int*. 2002;151(2):427–451.
55. Chapman M. Frequency-dependent anisotropy due to meso-scale fractures in the presence of equant porosity. *Geophys Prospect*. 2003;51(5):369–379.
56. Gurevich B, Makarynska D, de Paula OB, Pervukhina M. A simple model for squirt-flow dispersion and attenuation in fluid-saturated granular rocks. *Geophysics*. 2010; 75(6):N109–N120.
57. Song Y, Hu H, Rudnicki JW. Dynamic bulk and shear moduli due to grain-scale local fluid flow in fluid-saturated cracked poroelastic rocks: theoretical model. *J Mech Phys Solids*. 2016;92:28–54.
58. Shapiro SA. Elastic piezosensitivity of porous and fractured rocks. *Geophysics*. 2003; 68(2):482–486.
59. Toksöz MN, Johnston HD, Timur A. Attenuation of seismic waves in dry and saturated rocks: I. Laboratory measurements. *Geophysics*. 1979;44(4):681–690. https://doi.org/10.1190/1.1440969.
60. Pang M, Ba J, Carcione JM, Balcewicz M, Yue W, Saenger EH. Acoustic and electrical properties of tight rocks: a Comparative study between experiment and theory. *Surv Geophys*. 2022:1–31.

61. Hashin Z, Shtrikman S. A variational approach to the elastic behavior of multiphase materials. *J Mech Phys Solid*. 1963;11(2):127–140. https://doi.org/10.1016/0022-5096(63)90060-7.
62. Berryman JG. Single-scattering approximations for coefficients in Biot's equations of poroelasticity. *Acoustical Society of America Journal*. 1992;91(2):551–571.
63. Carcione JM. *Wave Fields in Real Media*. Elsevier; 2014.
64. Hashin Z, Shtrikman S. A variational approach to the theory of effective magnetic permeability of multiphase materials. *J Appl Phys*. 1962;33:3125–3131.
65. Mavko G, Mukerji T, Dvorkin J. *The Rock Physics Handbook: Tools for Seismic Analysis of Porous Media*. Cambridge University Press; 2009.
66. Osborn JA. Demagnetizing factors of the general ellipsoid. *Physical review*. 1945;67 (11-12):351.
67. Asami K. Characterization of heterogeneous systems by dielectric spectroscopy. *Prog Polym Sci*. 2002;27:1617–1659. https://doi.org/10.1016/S0079-6700(02)00015-1.
68. Archie GE. The electrical resistivity log as an aid in determining some reservoir characteristics. *Transactions of the AIME*. 1942;146(5):4–62. https://doi.org/10.2118/942054-G.
69. Aguilera MS, Aguilera R. Improved models for petrophysical analysis of dual porosity reservoirs. *Petrophysics*. 2003;44(1).
70. Wang Q, Chen D, Gao X, et al. Microscopic pore structures of tight sandstone reservoirs and their diagenetic controls: a case study of the Upper Triassic Xujiahe Formation of the Western Sichuan Depression, China. *Mar. Pet. Geol.* 2020;113 (Mar), 104119.
71. Pang M, Ba J, Carcione JM, Vesnaver A, Ma R, Chen T. Analysis of attenuation rock-physics template of tight sandstones: reservoir microcrack prediction. *Chin J Geophys*. 2020;63(11):4205–4219 (in Chinese).
72. Berryman JG. Long-wavelength propagation in composite elastic media. *J Acoust Soc Am*. 1980;68(6):1809–1831.